https://doi.org/10.1016/j.buildenv.2021.108234

Effects of wind direction and building array arrangement on airflow and contaminant distributions in the central space of buildings

Kai Yip Lee, Cheuk Ming Mak*

Department of Building Services Engineering, The Hong Kong Polytechnic University, Hong Kong

Abstract

Buildings are physical obstacles that diminish the benefits of wind by creating turbulence and reducing airflow velocities in urban settings. Particularly in the inner garden or amenities situated at the pedestrian level in the central space of a group of buildings, the efficiency of pollutant dispersion determines air quality and outdoor health. In this study, the effects of incident wind angles on wind velocity and pollutant distribution inside the central space of two building arrays arranged in 'L' and 'U' shapes were examined using computational fluid dynamics simulations. The 'L'-shaped array performed better than the 'U'-shaped array by forming a smaller low-wind-velocity (LWV) zone in the central space of the buildings (34.9%–76.11% of the total space). The 'L'-shaped array performed best at an incident wind angle of 225°, in which the LWV zone covered only 34.52% of the central space. A 90° incident angle produced the largest LWV zone (81.80%) for the 'U'-shaped array. The 'L'-shaped array generally distributed pollutants better than the 'U'-shaped array. However, the 'U'-shaped array with a 180° wind angle had a smaller high pollutant concentration area than the 'L'-shaped array with a wind angle of 225° ($K_c > 218.5$ covering only 0.37%). The worst vertical dispersion corresponded to a 135° wind angle for the 'L'-shaped array, which recorded the highest K_c at the mid-level of the building. In conclusion, the appropriate selection of building array designs and their orientations allows for the most effective use of wind flow to enhance ventilation and pollutant dispersion.

Keywords:

Airflow and contaminant dispersion
Building arrays
Building central space ventilation
Incident wind angles

*Corresponding author:
Department of Building Services Engineering, The Hong Kong Polytechnic University, Hung Hom, Kowloon, Hong Kong, China.

Email address: cheuk-ming.mak@polyu.edu.hk (Cheuk Ming Mak)

1. Introduction

Outdoor air quality and wind comfort in an urban environment have essential impacts on human health and have been frequently discussed in recent years. Factors such as wind velocity and airflow sufficiency play a vital role in diluting air pollutants generated from road traffic or other human activities. On the one hand, the complex interaction of atmospheric flow and airflow around buildings may hinder the dispersion of pollutants and affect the overall air quality in urban areas [1-4]. On the other hand, low wind speeds promote the accumulation of air contaminants inside street canyons and adversely affect outdoor air quality [5, 6]. Thus, insufficient ventilation and excessive penetration of outdoor air pollutants threaten the health of the occupants of buildings with natural ventilation [7]. Therefore, to dilute air pollutants in urban localities, outdoor ventilation within the building groups should be increased through careful town planning by considering the geometry of the urban setting [3, 8, 9].

Wind flow sufficiency enhances comfort and dilutes air pollutants. Higher wind speeds lower the concentration of contaminants due to better pollutant dispersion [6, 10-12]. However, the beneficial effects of wind are diminished and offset by the blockage effects from buildings or other urban structures [6, 13-15]. The effects of reduced wind speeds are particularly apparent in building wakes or within the central space of building groups. Moreover, atmospheric airflow also impacts the distribution of air pollutants on building surfaces, as inward and outward airflows are driven by the pressure differences produced by the wind or by buoyancy effects [16, 17]. Hence, indoor air quality in a naturally ventilated building is also affected. Thus, building shapes, the arrangement of building arrays, and incident wind angles influence environmental wind conditions and distribution in an urban environment.

Studies have thoroughly addressed wind flow around buildings, particularly at the pedestrian level [18-21]. Additionally, many computational fluid dynamics (CFD) studies address the prediction of pollutant concentration distribution around isolated buildings [4]. Buildings arranged in staggered patterns produce different blockage effects when compared with buildings arranged in a linear layout [6, 22, 23]. However, with the exception of a study on pollution dispersion at the pedestrian level inside the central space of building arrays, less attention has been given to inter-unit dispersion and vertical inter-unit dispersion [24, 25].Thus, the need for more studies on the CFD modeling of airflow and contaminant dispersions around building arrays is indicated [26] The impact of wind directions, and the shapes and orientations of the isolated buildings on the wind flow and velocities distribution around them has been investigated in other studies [27-30]. Further, studying the relationships among the different shapes and arrangements of obstacles or buildings in urban settings and incident wind angles is vital to identify their effects on the distributions of wind velocities in building wakes and the distribution of pollutant dispersion in the central space within building arrays.

Previous studies in Hong Kong determined that a mean wind speed of 1.5 ms^{-1} for 50% of the time at the pedestrian level provides the most comfortable environment during the summer months for pedestrians walking in the shade [31, 32]. Thus, areas with mean wind speeds lower than 1.5 ms^{-1} at pedestrian level (i.e., 1.75m in full scale) are considered low-wind velocity (LWV) zones that are uncomfortable and unfavorable for pedestrian activities [19]. Many residential buildings in Hong Kong are arranged in different shapes around a central space with a podium that includes recreational amenities (e.g., swimming pools, tennis courts, and playgrounds) [3]. Therefore, airflow penetration and pollutant dispersion at the pedestrian level in the central space or inner gardens of buildings significantly affects the health of those engaged in outdoor activities.

‘T’-shaped buildings and ‘U’- and ‘L’-shaped building arrays are quite common in urban areas of Hong Kong (Figures 1a–b). This study conducted comparisons of airflow patterns and wind velocities at the pedestrian level inside the central spaces of two types of building arrays (with different orientations) to maximize the benefits of natural ventilation and wind flow to favor pedestrian activities. The pollutant dispersion patterns inside the central space of the building arrays and on the building surfaces were also studied to identify the effect of the arrangement of building arrays and wind direction on pollutant dispersion. The turbulence model and computational settings were validated using wind flow data from the wind tunnel test results from the Compilation of Experimental Data for Validation Purposes (CEDVAL) project developed by the Meteorological Institute at the University of Hamburg [33]. The validated model and numerical settings were then used to simulate ‘U’- and ‘L’-shaped building arrays for different wind directions. As the wind flow pattern is closely related to the incident wind direction, five typical wind directions (depending on the arrangement of the building arrays) were selected and simulated using the validated CFD model. The airflow patterns, wind velocity distributions, and distributions of air contaminants inside the central space at the pedestrian level of the two building arrays are discussed in this paper. This finding considerably enriches the knowledge of orientation, building array arrangement, and pollutant dispersion capability and contributes to creating a livable and sustainable urban life.

Figure 1(a). 'T'-shaped building commonly found in Hong Kong arranged in 'U'- shaped pattern with the central space used as an amenity or inner garden (Source: Google Map)

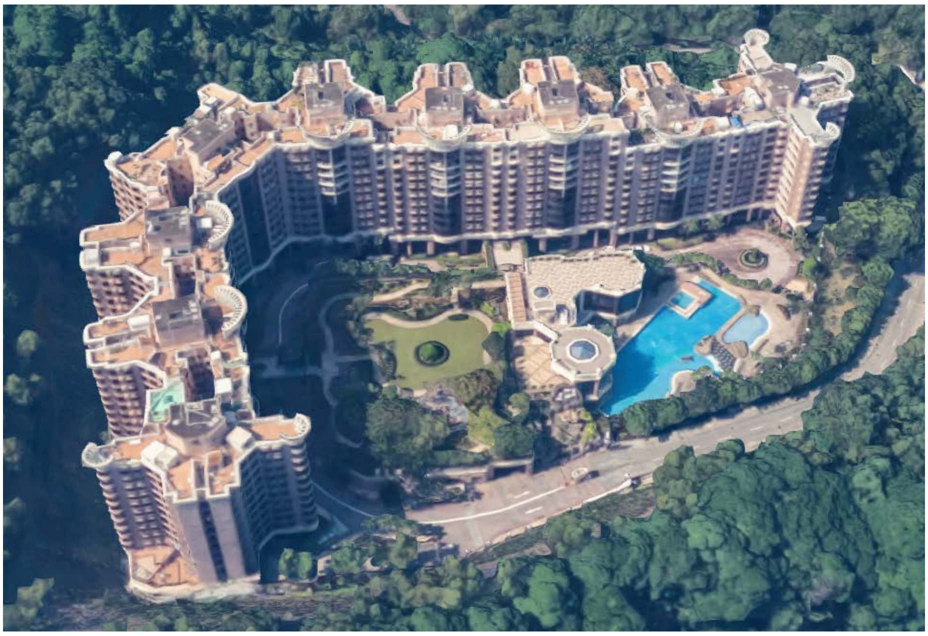

Figure 1(b). Residential buildings arranged in 'L'-shaped pattern with the central space used as an amenity or inner garden (Source: Google Map)

2. Methodology

2.1 CFD turbulence models

Identifying the concentration and dispersion patterns of air contaminants by conducting on-site measurements is a straightforward but expensive and often unfeasible approach for extended monitoring periods [3]. Numerical CFD methods, which provide complete field data with no similarity requirement limitations, offer an alternative manner to study the dispersion of air pollutants around a building [4]. An, Fung and Yim [34] used CFD to predict air velocities around single, double, and multiple building configurations in a detailed quantitative fashion. Experimental data, such as those from wind tunnel pollutant dispersion studies, are used to validate the simulated results.

Transient-state numerical models, such as large eddy simulation (LES) and direct numerical simulation (DNS), are more accurate and they could help reduce numerical errors because of the mean flow values obtained by taking time-average over a sufficiently long sampling period from the instantaneous ones and the discretization time steps [29, 35]. However, these methods are less popular for urban wind assessments as they are difficult in tuning and incurring much higher computational cost [28]. Xia, Niu and Liu [36] and Blocken [37] found that Reynolds-averaged Navier–Stokes (RANS) approaches, which focus on the mean flow properties of turbulence, are more commonly used to solve turbulence problems [36, 37], as they are less computationally expensive than the transient-state methods. Among different RANS approaches, An, Fung and Yim [34] found that the realizable k–ε model performs well for wind velocity prediction in high-wind regions, but it tends to underestimate the airflow in low-wind regions. However, the renormalization group (RNG) k-ε model provides consistent and accurate results when compared with wind tunnel flow and pollutant concentration field data [38-40].It also provides satisfactory results when studying wind-driven single-sided natural ventilation [41], and exhibits better performance for solving rapid strain and streamline curvatures. As such, the RNG k-ε model is more suitable for simulating urban wind flow [3, 42]. According to Du, Mak and Li [43], the adaptiveness of the RNG k-ε model is achieved by including an additional strain-dependent term (R_ε) as shown in Equation 1:

$$R_\varepsilon = \frac{C_\mu \rho \eta^3 (1 - \frac{\eta}{\eta_0})}{1 + \beta \eta^3} \cdot \frac{\varepsilon^2}{k} \qquad (1)$$

where C_μ, η_0, and β are constants (C_μ = 0.09, η_0 = 4.38, β = 0.012), ρ is the fluid density, *k* is the turbulent kinetic energy, *ε* is the turbulent viscous dissipation rate, and $\eta \equiv Sk/\varepsilon$ where *S* is the strain rate scale. According to the ANSYS code [44], the revised feature in the RNG *k*–*ε* model permits effective flow prediction with low Reynolds (*Re*) numbers in near-wall regions. The RNG *k*–*ε* model was selected for the validation process with CEDVAL wind tunnel data due to its availability, consistency, and suitability.

2.2 Wind tunnel experiment and model validations

The experiment was conducted in the 'BLASIUS' wind tunnel [33] at the Meteorological Institute of the University of Hamburg. It is an open circuit wind tunnel that draws air from the room and exhausts inside the same room. The buildings were constructed and modeled at a scale of 1:200. Before the building models were mounted in the test section, the boundary layer flow was validated based on detailed flow measurements. The 3 × 7 array of buildings consisted of rectangular blocks. 2D flow measurements were performed in four vertical and one horizontal measurement plane. Emission data were acquired within one horizontal measurement plane at a height of Z = 1.5 m (full scale). Four ground-level CO_2 emission sources were mounted close to the building (Figure 2). Flow and CO_2 dispersion were measured within the street canyon, downwind of the building equipped with the sources (Figure 2). The concentrations are shown in a dimensionless form using Equation 2:

$$K_c = \frac{C_{measured}}{C_{source}} \frac{U_{ref} H^2}{Q}, \qquad (2)$$

where $C_{measured}$ is the measured tracer concentration in ppm (previously subtracted background concentration), C_{source} is the tracer concentration in ppm at the sources, U_{ref} is the reference wind speed in m/s measured at H = 0.66 m, H is the model building height (H = 0.125 m), and Q is the total source strength in m^3/s.

Wind tunnel tests from the CEDVAL project, developed by the Meteorological Institute at the University of Hamburg Environmental Wind Tunnel Laboratory [33] were employed to validate our models (Figure 2). We constructed models at a 1:200 scale (unit volume with side H = 0.125 m) for direct comparison with the CEDVAL wind tunnel project. Table 1 lists the test parameters. The similarity requirements between the wind tunnel and CFD models were strictly tested. The *Re* number was greater than 3.7×10^4, which achieves the minimum requirement of 1.5×10^4 suggested by Meroney [45], thus attaining *Re* independence and fulfilling the similarity requirements.

Table 1. Parameters for the scaled model

Parameter	Symbol	Value
Building height	H	0.125 m
Reynolds number	Re	37, 252
Power law	$\acute{\alpha}$	0.21
Reference velocity	U_{ref}	6.3 m/s
Reference height	H_{ref}	0.66 m
Friction velocity	$u*$	0.37772 m/s
Roughness length	z_0	0.00075 m
Offset height	d	0.00 m
Turbulence length	L	0.32 m

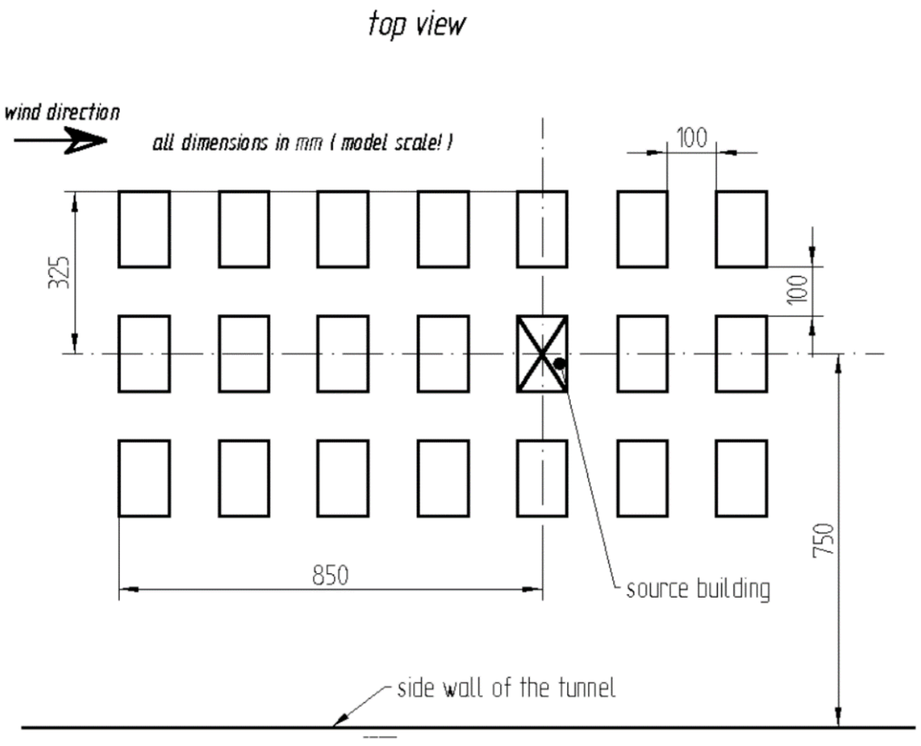

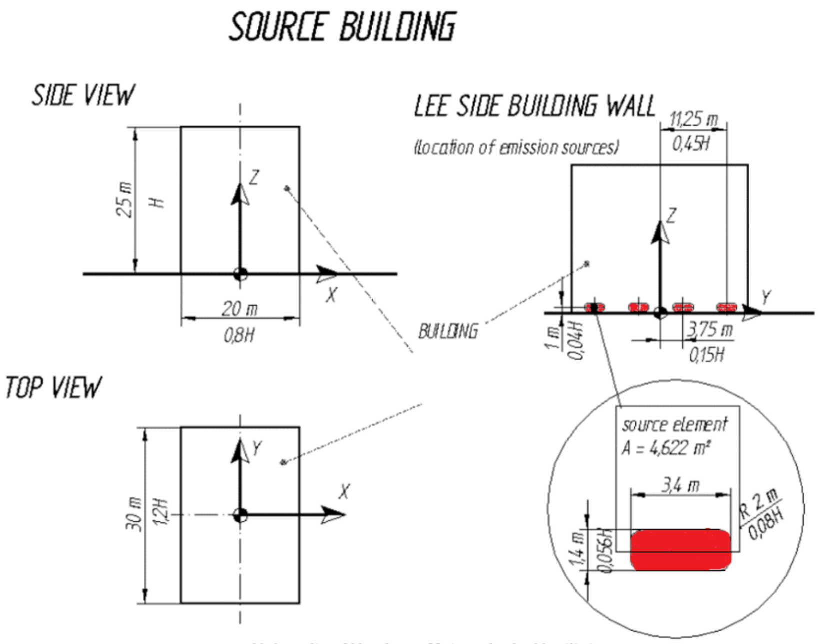

University of Hamburg, Meteorological Institute

Figure 2. Setup sketch of the wind tunnel showing the building arrangement, location of the source building and measurement points. The areas highlighted in red are the emission points.

Inhomogeneous atmospheric boundary layer (ABL) generally refers to a mismatch between the inlet and incident ABL profile [46]. It shows streamwise gradients in vertical velocity and turbulence profiles throughout the computational domain [47]. The inhomogeneous ABL and near-wall treatments significantly affect the atmospheric flow and pollutant dispersion simulation results [47]. On the other hand, homogeneous ABL ensures that the wind conditions acting on the building are identical to those intended by the modeler [46], and it happens when the turbulence model, inlet conditions and law applied to wall roughness are consistent [47]. Hence, an accurate simulation of the flow and dispersion of air pollutants requires the development of a homogeneous ABL before conducting numerical studies.

To fully develop a horizontally homogeneous ABL flow and to achieve equilibrium between the turbulence dissipation and production, the domain inlet boundary conditions are represented by the profile of mean wind velocity U_z, the turbulent kinetic energy k, and turbulent dissipation rate ε, as expressed in Equations 3, 4, and 5, respectively.

$$U_{(z)} = \frac{u^*}{K} ln\left(\frac{z + z_0}{z_0}\right) \tag{3}$$

$$k = \sqrt{C_1 \, ln(z + z_0) + C_2} \tag{4}$$

$$\varepsilon = \frac{u^*\sqrt{C_\mu}}{K(z+z_0)}\sqrt{C_1 ln(z+z_0)+C_2} \tag{5}$$

This set of inlet boundary conditions, when incorporated into an appropriate near-wall treatment on the domain ground, permits a homogeneous ABL [47, 48]. From the above equations, $U_{(z)}$ is the average wind speed at height z above the ground, z_0 is the roughness length (0.00075 m), $u*$ is the frictional velocity (0.37772 ms^{-1}); C_1 and C_2 are constants equal to 0.025 and 0.41, respectively; C_μ is a constant equal to 0.09; and K is the von Karman constant, which is equal to 0.4187 according to Ai and Mak [5].

The downstream vertical boundary was modeled as an outflow. The sky was treated as a mirror plane. An enhanced wall function was adopted for the building block surfaces, where the computational domain was non-slip. The mesh near the building and ground surfaces was refined to replicate the physical characteristics of the flow. Horizontal homogeneity was required to accurately simulate the approaching ABL flow in the computational domain; thus, the vertical flow profiles prescribed at the inlet had to be preserved in the domain before reaching the buildings [49].

The low-Reynolds-number regions below the first grids and the effects on the entire wall-bounded flow can be ignored, as the standard wall functions directly link the walls and near-wall logarithmic layer with a series of semi-empirical formulae [47]. In the present study, an enhanced wall treatment (which integrated the flow variables down to the walls) adopted for near-wall modeling resolved the viscous sublayer and computed the wall shear stress from a local velocity gradient normal to the wall. Additionally, the treatment more accurately predicted the velocity distributions in the recirculation zones near the windward edges and in the building wakes [38]. The computational domain was built using hexahedral elements with a finer resolution close to the ground and the regions where the plume was evolving. In this study, a relatively fine mesh was imposed in the wall-normal direction (i.e., a small y^+ value between 2 and 5) to demonstrate the suitability of the selected grid for the enhanced wall treatment.

To ensure fully developed wind flow with minimum blockage effect, the upstream, downstream, lateral, and height components of the computational domain were set as 5H, 15H, 3.4H, and 3.4H, respectively (Figure 3), based on CFD practice guideline requirements [50]. However, the lateral distance was adjusted based on the wind tunnel width to ensure accurate reproduction. The blockage ratio was approximately 1.7%, conforming to the European Cooperation in Science and Technology (COST) Action 732 requirement [50]. The entire domain was constructed using structured hexahedral grids with a grid expansion ratio of 1.2 in the horizontal and vertical directions, as in the research of Tominaga et al. [51]. The pressure and momentum equations were coupled using the semi-implicit method for pressure-linked equations (SIMPLE) algorithm, and a second-order upwind scheme was used in the discretization. The scaled residuals in the simulation were all set to 10^{-5}, and convergence was obtained at this level.

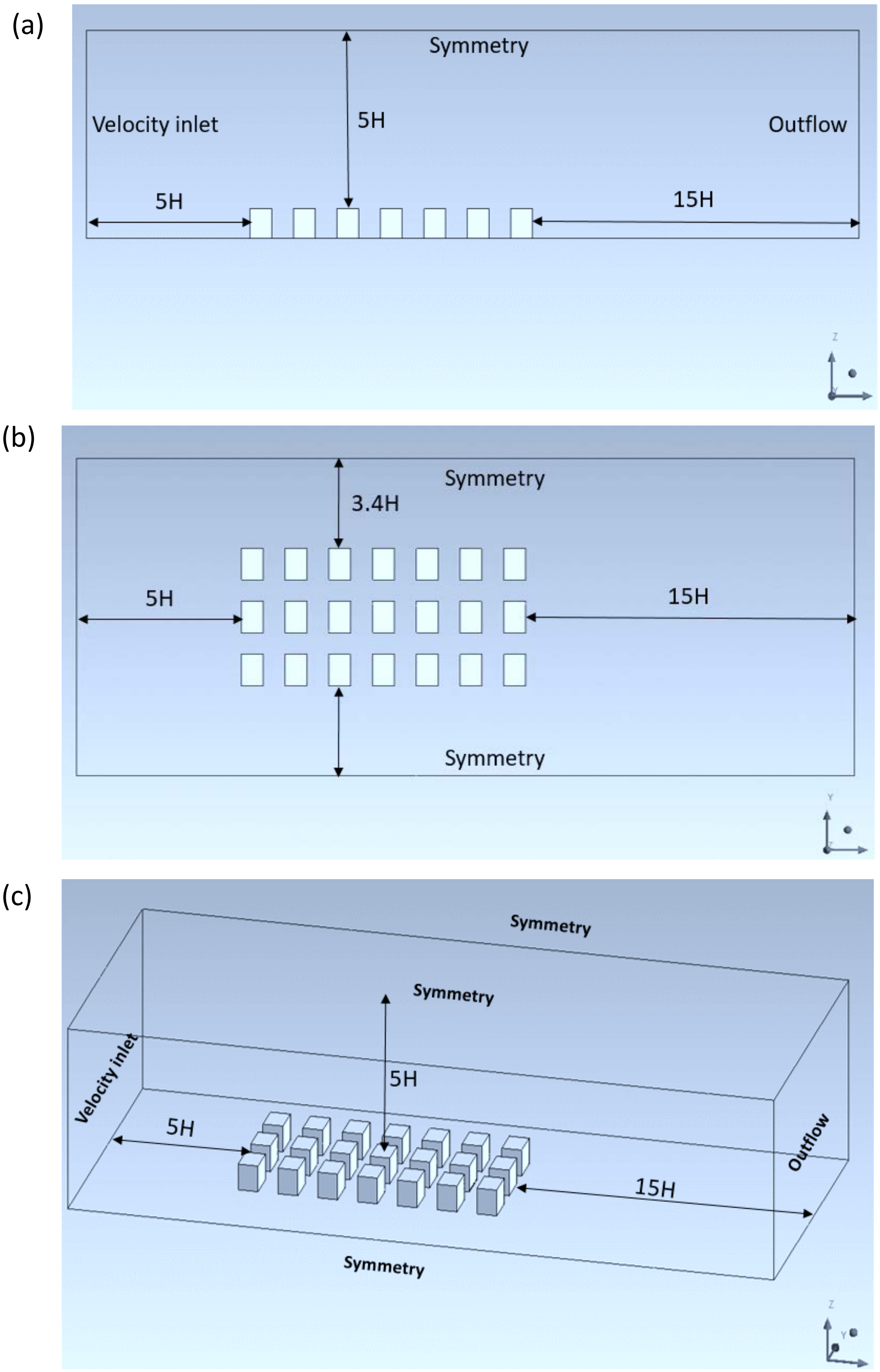

Figure 3. Computational domain of the 3 × 7 array of buildings in the wind tunnel.

Grid-sensitivity analyses are performed to reduce discretization errors and computational time [52]. In this study, a grid-sensitivity analysis was performed based on three constructed mesh systems, with minimum grid sizes of 0.0005 m, 0.0002 m, and 0.00005 m and mesh numbers of 2.75 million (coarse), 5.86 million (moderate), and 8.35 million (fine), respectively (Figure 4). The simulation results from the three systems were compared to examine the independence of the numerical solution with respect to the grid size. The $y+$ values of the first near-wall grids in the vicinity of the building surface and the ground were less than five (i.e., $y+ = 4.23$) for a minimum grid size was 0.0002 m. For the mesh systems with the minimum grid sizes of 0.0005 m (coarse mesh) and 0.00005 m (fine mesh), the $y+$ values were 10.57 and 1.05, respectively. Correlation coefficient (R^2) and geometrical mean bias (MG) values closer to 1 improve the predictive ability of the model [43].

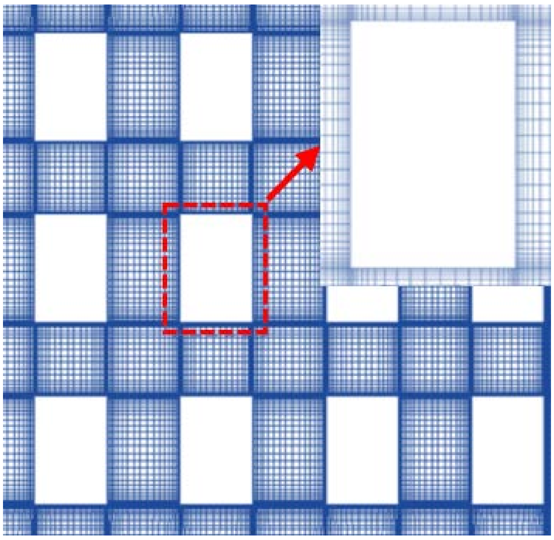
(a)

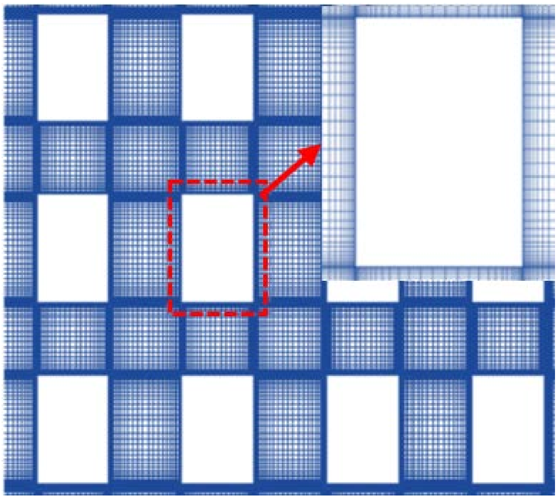
(b)

(c) 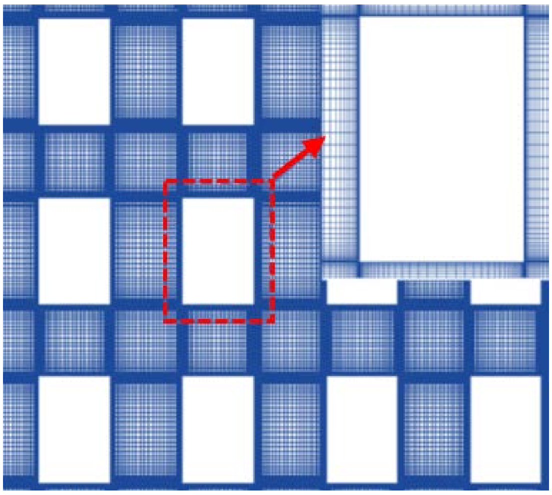

Figure 4. Mesh resolution of the three systems: (a) coarse mesh with the minimum grid size of 0.0005 m; (b) moderate mesh with the minimum grid size of 0.0002 m; (c) fine mesh with the minimum grid size of 0.00005 m.

Figure 5 shows a comparison of the non-dimensional wind velocity ratio (U/U_{ref}) (U_{ref} is 6.3 m/s) at the reference height (H_{ref}) of 660 mm from the wind tunnel experiment with the results of the simulated RNG model with different mesh systems arranged in coarse (C), moderate (M), and fine (F) grids. Figure 5 shows that the coarse mesh generally underestimated the wind velocity at all points along the y-axis; relatively accurate results were obtained using the moderate and fine meshes. Table 2 lists the correlation coefficients of the results generated using different mesh systems, all of which showed good correlation with the experimental data; the fine mesh had the best result (0.999), followed by the moderate mesh (0.997). However, the moderate mesh (M) yields better MG results closer to 1. Considering the accuracy and expenditure of computational resources, a moderate mesh system with a minimal grid size of 0.0002 m was adopted.

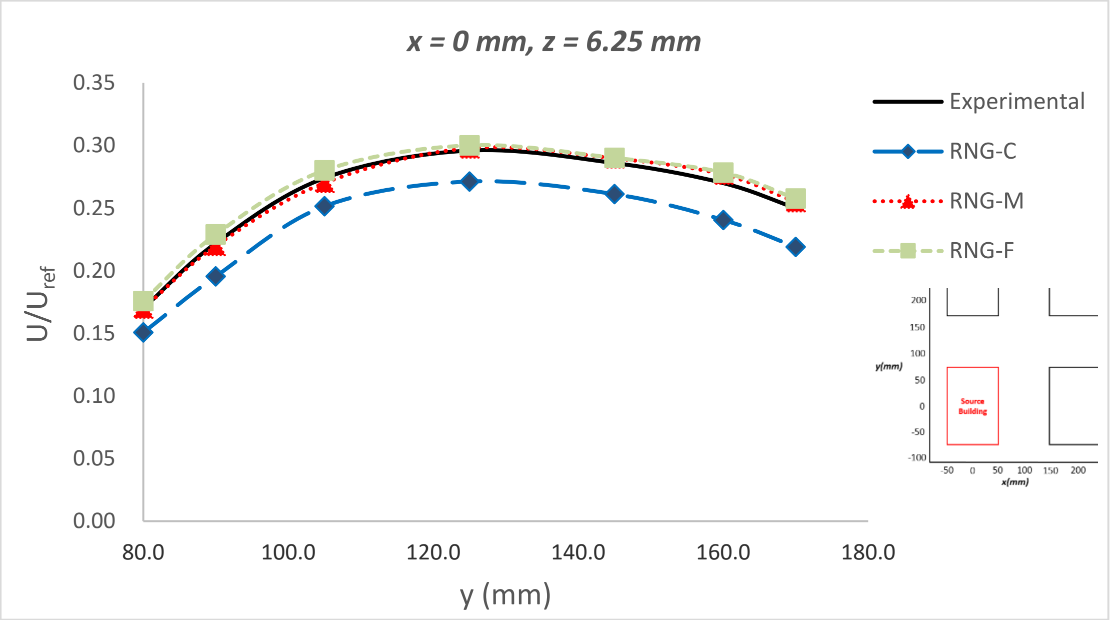

Figure 5. Comparison of the wind tunnel data with the simulated RNG k-ε models with coarse (RNG-C), moderate (RNG-M), and fine (RNG-F) mesh systems.

Table 2. Statistical test results of the RNG k-ε models with three different mesh systems.

Statistical Tests	RNG-C	RNG-M	RNG-F
Correlation Coefficient (R^2)	0.996	0.997	0.999
Geometric Mean Bias (MG)	1.112	0.994	0.976

Figure 6 compares the wind velocity ratio of the mid-level of the building model from the wind tunnel data sets and the modeled results using the RNG *k*-ε model with a moderate mesh system. Figures 6(a) and 6(c) show that the RNG model with a moderate mesh system accurately predicted the wind velocity distribution in the building wake despite slightly underestimating the wind velocity distribution in the center of the street canyon (Figure 6(b)).

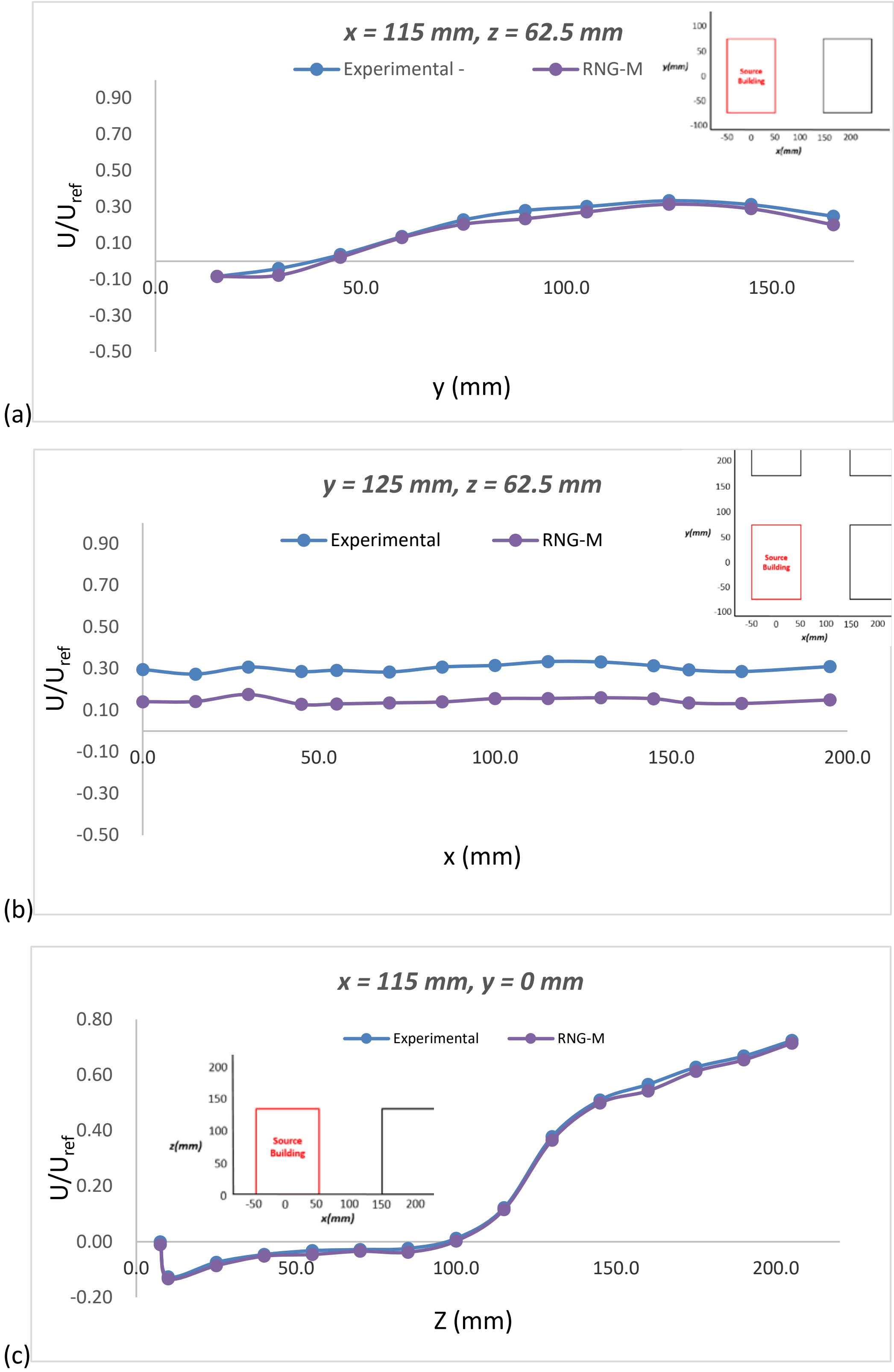

Figure 6. Mean wind velocity distribution for moderate mesh system by RNG as RNG-M at different sampling locations.

Figure 7 displays the tracer gas concentration distribution from the wind tunnel experiment and the CFD simulation from the RNG model with the medium mesh system (minimum grid size of 0.0002 m). The measurements were conducted at the pedestrian level (i.e., 1.75 m in full scale) on the leeward wall near the emission points. The simulated results near the emission area (i.e., x = 50 mm) contained noticeable differences between the experimental wind tunnel data and the modeled data. However, the remaining model results deviated only subtly from the experimental results. Therefore, this model is considered accurate and appropriate for the current study.

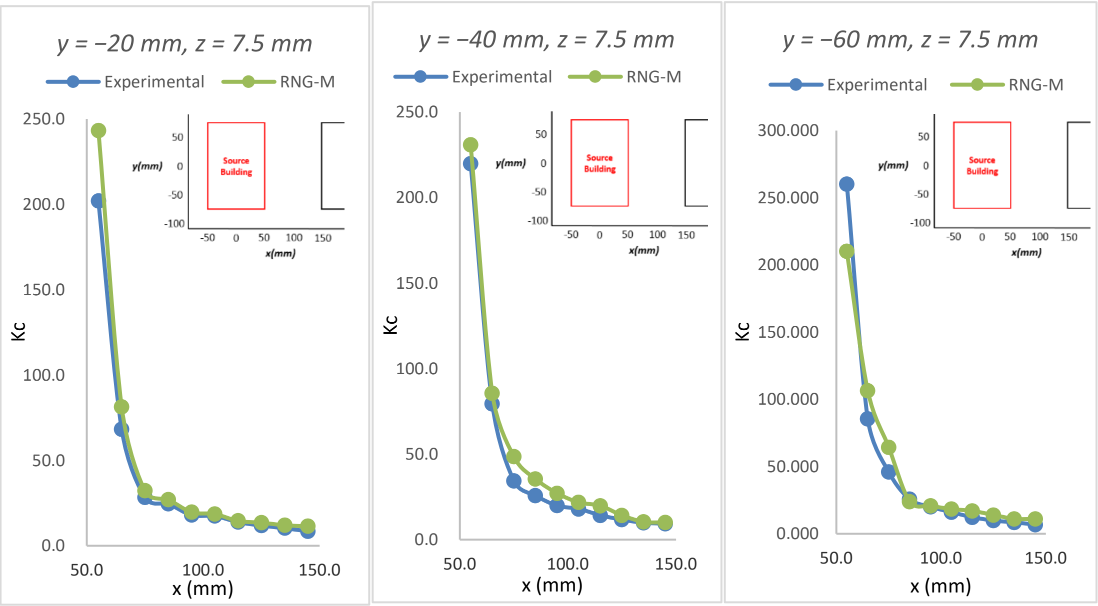

Figure 7. Tracer gas concentration distribution for moderate mesh system by RNG as RNG-M at different sampling locations.

3. Description of building configuration and arrays

The authors studied a very common building configuration (i.e., ‘T’-shaped) in Hong Kong during a pilot study in an isolated building setting and found that the vortex formed near the protruding structure in the back section on the leeward of the ‘T’-shaped building helped shorten the horizontal spread of the zero- and low-wind velocity zones in the building wake [30]. The resulting high-velocity flow on the leeward side penetrates more deeply into the street canyon and facilitates the dispersion of air pollutants in the building wake [30]. Two common building arrangements (i.e., the computational domains for ‘L’- (Figure 8(a)) and ‘U’-shaped (Figure 8(b)) were selected to further study the effects of ‘T’-shaped arrays and incident wind angles on wind velocity distribution and pollutant dispersion in building wakes.

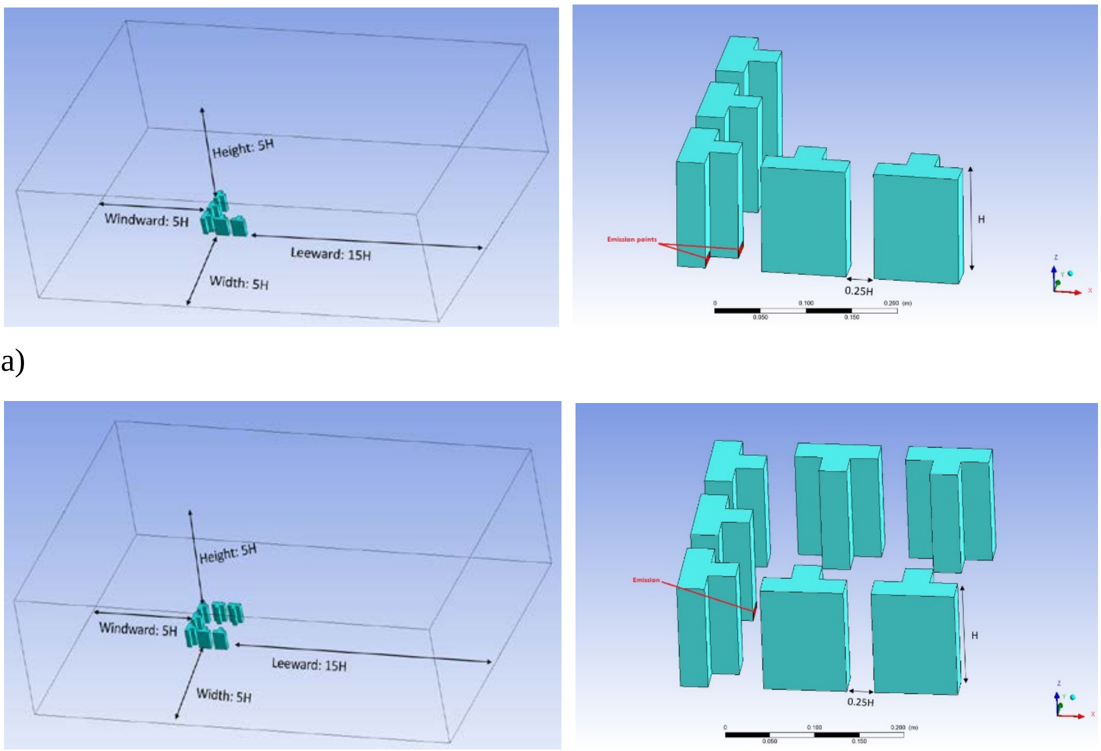

(a)

(b)

Figure 8. The computational domains for (a) 'L'-shaped array; and (b) 'U'-shaped array.

The effects of different wind angles, including direct wind (θ = 0°), oblique approaching wind (θ = 45°), oblique opposing wind (θ = 135°), lateral wind (θ = 90°), and opposing wind (θ = 180°) (see Figures 9(a) and 9(b)) were investigated. An oblique opposing wind at θ = 225° was also studied in an 'L'-shaped array (see Figure 9(a)). The above-discussed validated mesh, inflow wind profile, computational domain size, turbulence model, and numerical methods were used for the wind flow simulation around the two building arrays. The moderate mesh system with a minimum grid size of 0.0002 m and about six million grids was adopted in the computational models of the investigated cases of the two building arrays. Mean wind flow velocity ratios of less than 0.25 are deemed uncomfortable and unfavorable for pedestrian activities. Mean wind velocity ratios distributions at the pedestrian level (1.75 m at equivalent full scale) in the building wakes were calculated to determine the areas of unfavorable conditions for pedestrian activities. The central space to be studied is an imaginary rectangular area that covers most of the area in the middle of the building arrays, and is bounded by the mid-lines of the farthest buildings (see Figures 9a and 9b). Color summarizing software (http://mkweb.bcgsc.ca/color-summarizer/?analyze) was used to assess the percentage of the area classified as the LWV zone in the central space inside the building arrays using the color distributions in Figure 10.

In addition to the airflow and ventilation distributions, this study modeled the release of tracer gas (CO_2) from the elements of the source building with a constant velocity of 0.025 m/s in the X direction toward the central space of the building arrays to simulate pollutant dispersion. The total area of the emission points is the same as that in the wind tunnel model (CEDVAL B1-1) to mimic the exact flow rate and volume of released tracer gas. The distributions of the pollutant concentration expressed in a dimensionless concentration, K_c, were deduced using Equation 2.

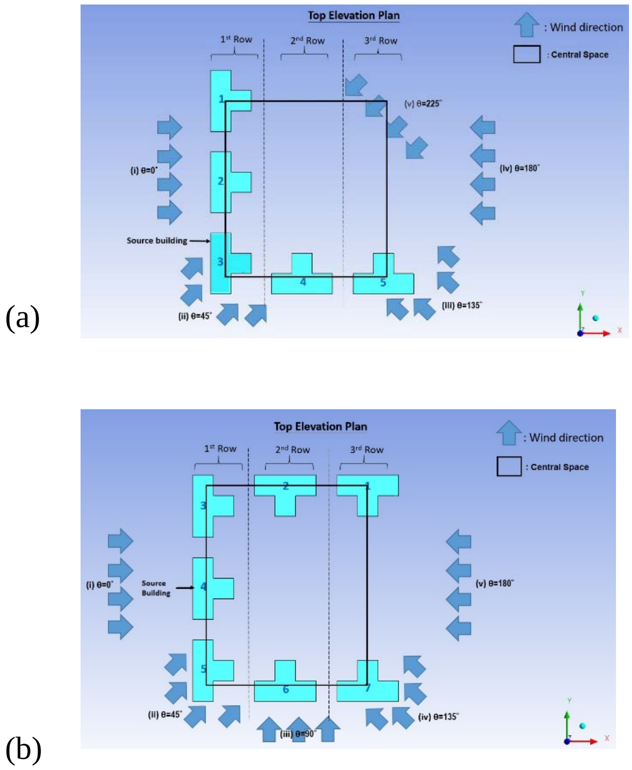

Figure 9. Identification of building blocks, building arrays, and incident wind directions: (a) 'L'-shaped arrangement; (b) 'U'-shaped arrangement. The black rectangle shows the location and boundary of the central space.

4. Results and discussions

4.1 Distribution of airflow inside the central space of building arrays

Figure 9 shows the general features of the wind velocity ratio (U/U_{ref}) distribution around 'T'-shaped buildings in an 'L'-shaped array at the pedestrian level under different incident wind directions to assess pollution levels and pedestrian thermal comfort. The five prescribed wind directions had different velocity distribution patterns and low-wind zone developments in the building wake and the central space of the building array.

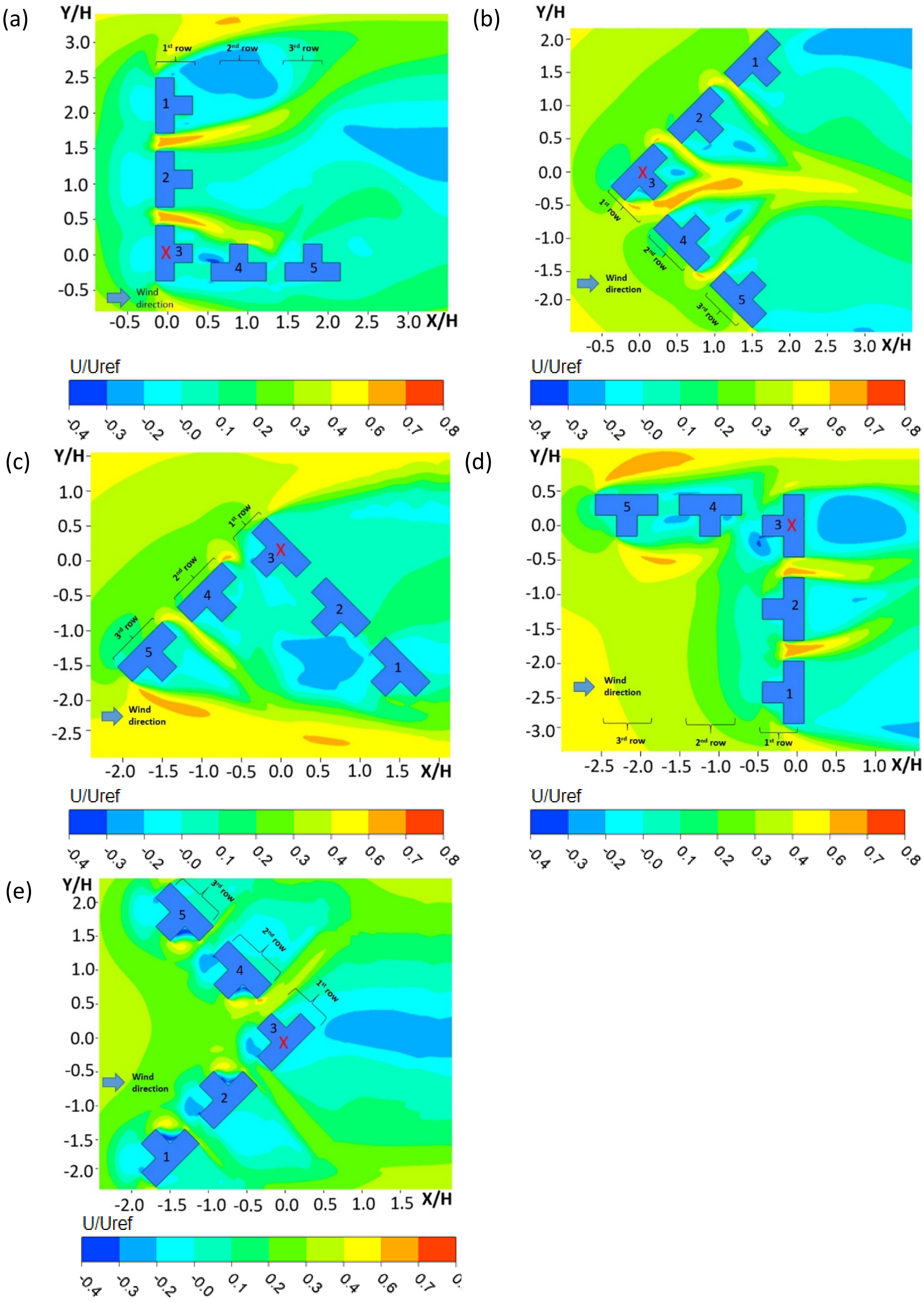

Figure 10. Distributions of velocity ratio (U/U$_{ref}$) in the horizontal plane at the pedestrian height (8.75 mm in scaled model, 1.75m in full scale) for 'L' arrangement with incident wind angles of: (a) 0°, (b) 45°, (c) 135°, (d) 180°, and (e) 225°.

The area of the LWV zone in the central space of the building array was generally the largest (76.11%) for wind hitting the surface of the 1st row of buildings (Figure 10(a)). The LMV zone covered 71.42% of the area of the central space for a wind angle of 90° Figure 10(c). The situation in Figure 10(b) shows slightly improved air velocity distribution and an LWV zone covering less than 65% in the central space. The wind infiltrated through the slits in the buildings to reach the central space. In the case presented in Figure 10(c), the air infiltrates the building gaps; additionally, airflow and vortex development were impacted by Blocks 1 and 2 in the 1st row, causing stagnation of air inside the central space. The cases in Figures 10(d) and 10(e) demonstrate better ventilation inside the central space of the 'L'-shaped building array. The LWV zone in Figure 10(d) covers 51.78% of the central space and is less favorable than the LWV zone Figure 10(e), which covers only 34.52%. Both cases show that the central spaces of the building arrays were facing the wind direction; however, the 1st row of buildings in Figure 10(d) gradually reduces the air velocity passing through the central space by blocking the airflow. Figure 10(e) shows that the air velocity was drastically reduced when the wind approached the surface of the building from an oblique incident angle. Therefore, the case in Figure 10(e) is the most ideal wind velocity and outdoor ventilation for the central space in the 'L'-shaped building array.

Figure 11 illustrates the airflow pattern and velocity distribution inside the central space of the 'U'-shaped building arrays, which appeared as a semi-enclosed arrangement of the buildings. Figure 11 shows that the 'U'-shaped array did not perform as well as the 'L'-shaped array in terms of ventilation and air penetration. Depending on the incident wind angles, the LWV regions occupied 60.71%–81.80% of the central space of the building array. Figure 11(c) shows the worst situation, where only 18.20% of the total area inside the central space demonstrated satisfactory airflow (i.e., $U/U_{ref} > 0.25$). Wind flow approaching the building array from 90° hits Blocks 5, 6, and 7; and the airflow enters the central space. The decelerated air reached Blocks 1, 2, and 3 after passing through the first half of the central space and formed a vortex, which further slowed the air inside the central space and produced the worst-case airflow velocity distribution scenario. Two cases with oblique incident wind angles (i.e., 45° and 135°) performed slightly better, and the LWV zone occupied 74.97% and 73.07% (Figures 11(b) and 11(d), respectively). The case shown in Figure 11(b) is slightly better than that in Figure 11(d), because the wind passes through the slits of the buildings at a 45° rotation and moves freely through the opening of the semi-enclosed arrangement of the 'U'-shaped arrays; the air recirculation and vortex formed in front of Blocks 1, 2, 3, and 4 (Figure 11(d)) reduced the airflow velocity inside the central space of the building array. Finally, the 180° angle (Figure 11(e)) was expected to be the best, because the opening of the semi-enclosed feature of the building array exposed the central space to the incoming wind and allowed more throughflow. However, Figure 10(e) performed better, because the wind in Figure 11(e)) directly horizontally impacted Blocks 3, 4, and 5; thus recirculation and vortex formation again slowed the incident wind. In contrast, the wind in Figure 10(e) approached the central space and hit the building blocks at an oblique angle; thus, air velocity and turbulence dissipated very quickly near the windward walls of the buildings. The resulting vortex was not large enough to slow down the airflow reaching the central space of the building group.

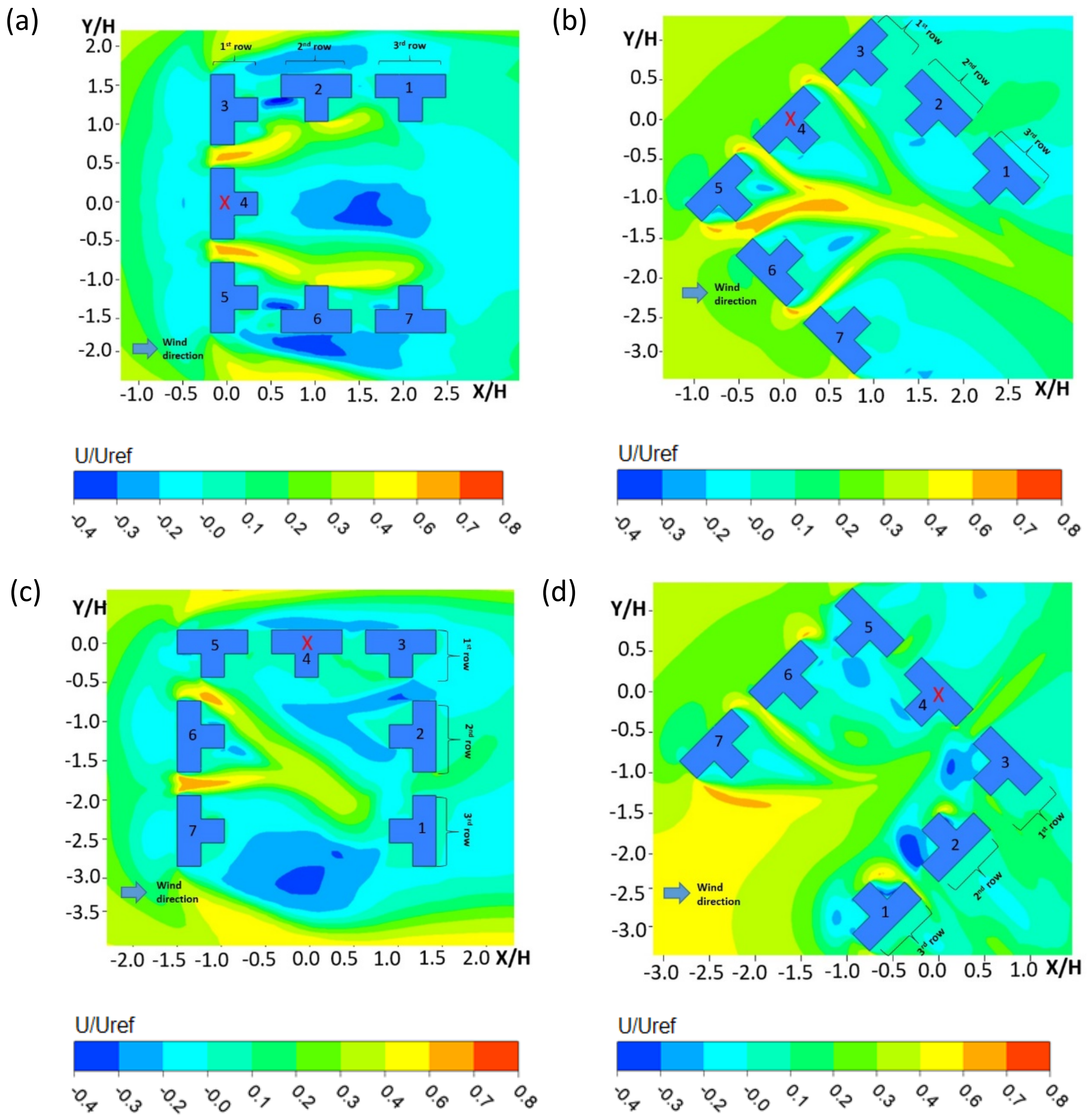

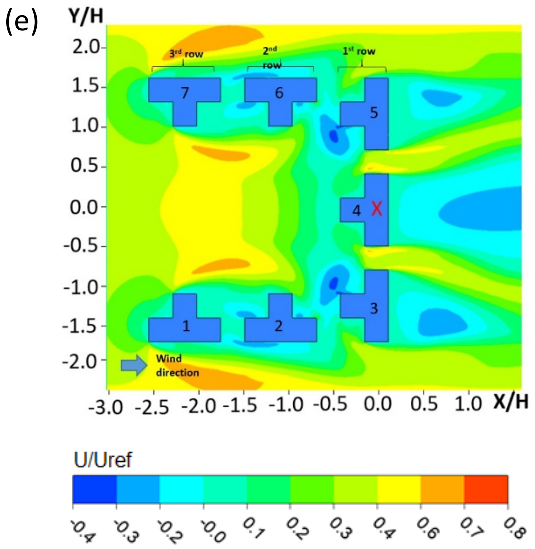

Figure 11. Distributions of U/U_{ref} in the horizontal planes at a pedestrian height (8.75mm in scaled model and 1.75 m at equivalent full scale) for the 'U' arrangement with incident wind angles of: (a) 0°, (b) 45°, (c) 90°, (d) 135°, and (e) 180°.

To summarize, the 'L'-shaped building array performed better than the 'U'-shaped array; and oblique wind angles effectively helped maintain airflow penetration and good ventilation within the central space of the building array. In addition, openings in semi-enclosed features of the building arrays that were located downstream from the airflow created a favorable ventilation conditions and maintained sufficient wind velocity inside the central space. However, openings in the building array enclosure that were located in an upwind position stopped airflow from reaching building groups situated downstream and perpendicular to the wind direction. Thus, the turbulence and recirculation of airflow created LWV zones within the central space of the building arrays, making them less favorable for pedestrian activity.

4.2 Air contaminant dispersion inside the central space of building arrays

To assess the dispersion of air pollutants inside the central space of the building arrays, a simulation of the tracer gas (i.e., CO_2) in the vents from the source building was conducted. Figure 12 shows the contours of the time-averaged dimensionless concentration of tracer gas inside the central space of the 'L'-shaped building array.

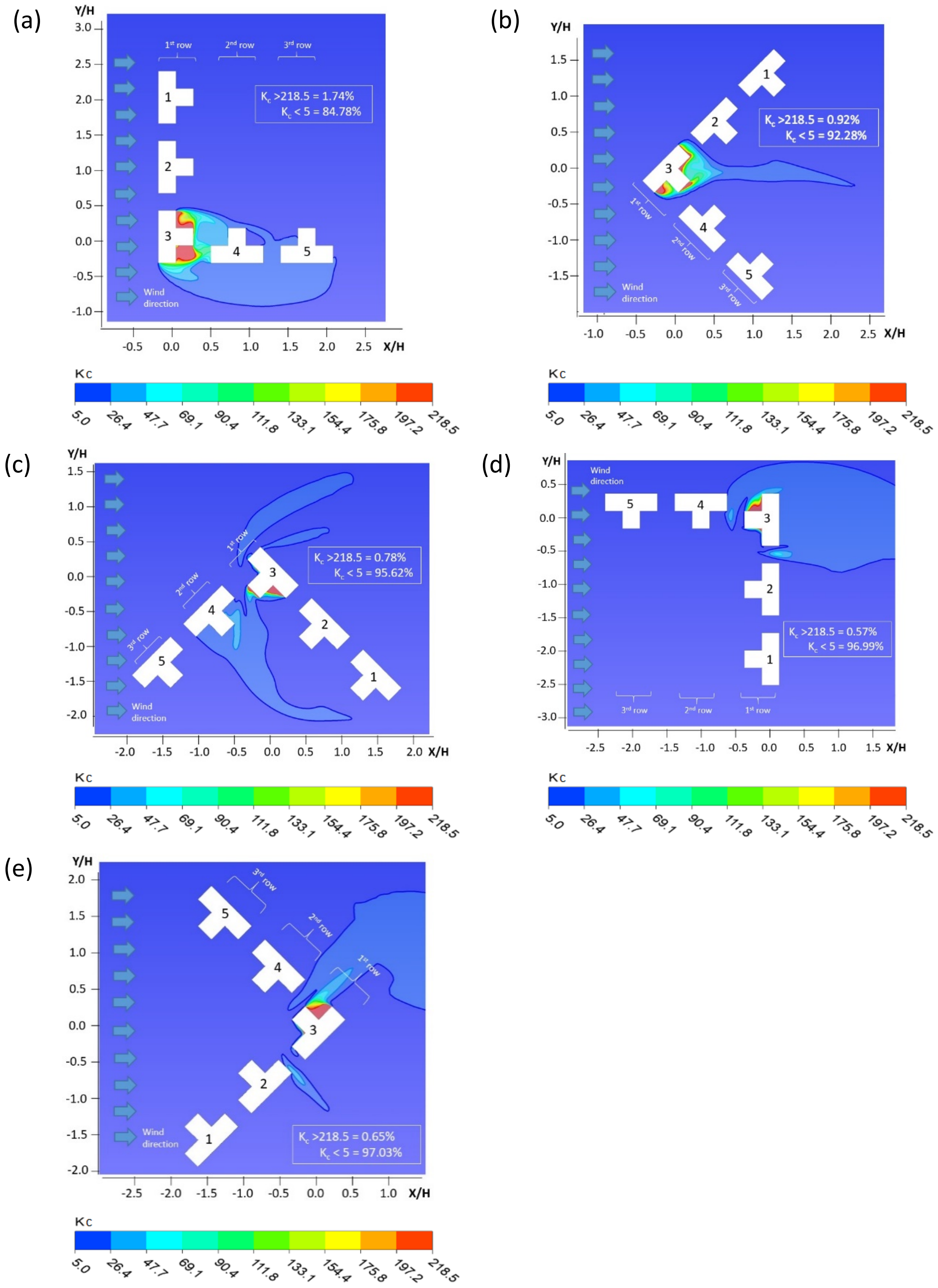

Figure 12. Concentration distribution of the 'L'-shaped arrangement with incident wind angles of: (a) 0°, (b)45°, (c)135°, (d) 180°, and (e) 225°, at pedestrian height (8.75 mm in scaled model, 1.75m in full scale).

A distinct high-concentration area ($K_c > 218.5$) appeared near the emission vents in the source building. The tracer gas emitted from the source building was transported downstream by the air current, decreasing the pollutant concentration in the downstream regions. As the tracer gas was transported by the airflow, the emissions did not affect buildings and/or the central space of the building group located in the upstream position. The enclosure opening of the building array and the central space were facing the wind direction, which minimized the effect of the tracer gas emissions and air pollutant on the central space of the building array (Figures 12(d) and 12(e)). Figure 12(d) shows that the ratios of the heavily polluted area ($K_c > 218.5$) and least polluted area ($K_c < 5$) were 0.57% and 96.99%, respectively. These values are quite similar to those shown in Figure 12(e), where the ratios of heavily polluted areas and least polluted areas are 0.65% and 97.03%, respectively. Contaminants accumulated behind the protruding part of the 'T'-shaped building (later referred to as the 'Middle Block') for oblique angle wind directions (Figure 12(e)). However, as the source building was located in the downwind position under this wind direction, air pollutants had the least impact on the central space of the building array, making it more suitable for pedestrians or amenities. Figure 12 (d) shows that the airflow and vortex development were impacted by Blocks 1 and 2 in the 1st row for an oblique wind angle of 135°, which caused air stagnation in the central space. Consequently, the pollutant was not efficiently dissipated and accumulated in the central space of the building array.

For an oblique wind angle of 45°, the high wind velocity inside the central space facilitated the dispersion of air pollutants, creating steeper and denser pollutant concentration contours (Figure 11(b)); additionally the heavily polluted area occupied approximately 0.92% of the central space. For an approaching wind angle of 0°, the blockage effect of Block 3 created air turbulence in its wake, and the low wind velocity in the wake further hindered emission dissipation. Consequently, the pollutant lingered around Blocks 4 and 5, heavily polluting 1.74% of the total area.

As the enclosure opening was narrower in the 'U'-shaped arrays than in the 'L'-shaped ones, more air pollutant accumulation was expected in the central space of the 'U'-shaped array (Figure 13). Figure 13(a) shows the worst dissipation of air pollutants in the central space of the building array (and the largest area ratio of 1.63%). The high pollutant concentration was attributed to air turbulence and vortices formed in the wakes of the 1st row of buildings. Building blocks in the 2nd and 3rd rows on both sides helped stabilize the atmosphere in the horseshoe-shaped central space, allowing slow, gradual, and symmetrical dissipation of the tracer gas throughout the central space, as manifested by the wide and even contour lines. In Figure 13(b), the source building was located on the left-hand side of the wind flow; whereas the opening of the semi-enclosed array was located downstream of the emission source, which allowed the airstream to carry the pollutants through the opening of the semi-enclosed structure of the building array. Thus, pollutant emissions did not significantly affect the downstream buildings. However, in the case shown in Figure 13(c), Block 3 is located in the wake of the source building (Block 4) that created a blockage effect and air turbulence between the buildings and discouraged the dissipation of air pollutant, which lingered between the spaces of the two buildings. The area ratio of high pollutant concentration was approximately 1.09%, and the least polluted (i.e., $K_c < 5$) area (84.86%) was the lowest among all the ‘U’-shaped arrays. Because the openings of the semi-enclosed structure of the building array in Figures 13(d) and 13(e) were facing the incident wind, the emission points were located downstream of the central spaces; thus, the afore-mentioned incident wind angles had less impact on the accumulation of air pollutants in the central space of the building arrays. The area ratios with high pollutant concentrations in Figures 13(d) and 13(e) were 0.69% and 0.37%, respectively; and the lowest pollutant area ratio in both cases exceeded 93% in the central space. Thus, incident wind angles of 135° and 180° were the best for pollutant dissipation in ‘U’-shaped building arrays. However, the 180° and 225° cases in the ‘L’-shaped building arrays had larger least-polluted area rations (i.e., $K_c < 5$).

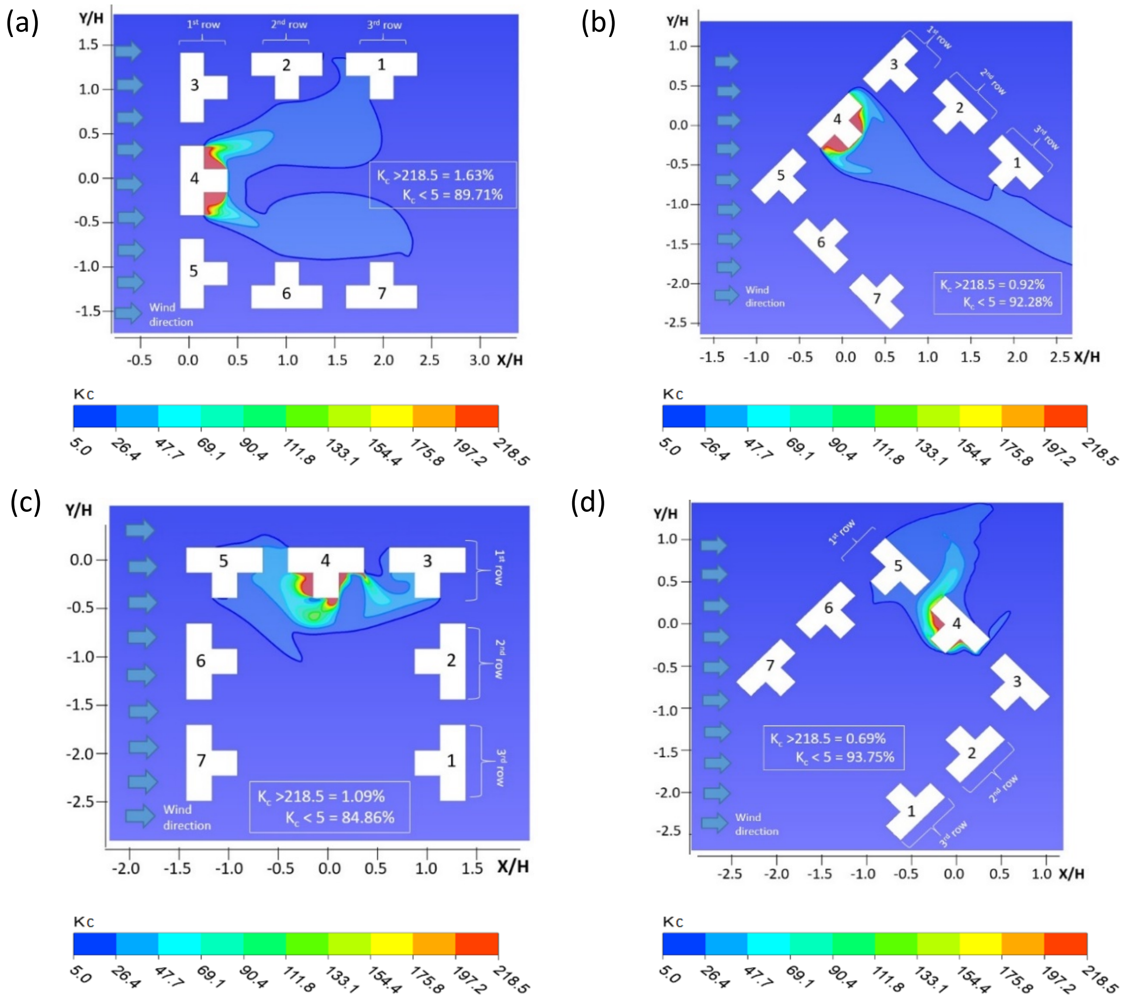

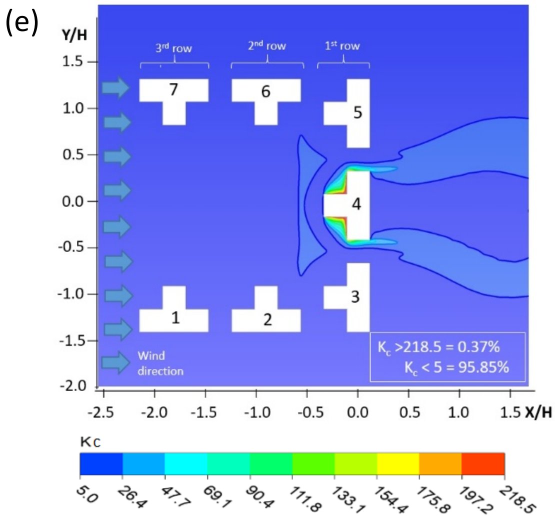

Figure 13. Concentration distribution for 'U' arrangement with incident wind angles of: (a) 0°, (b) 45°, (c) 90°, (d) 135°, and (e) 180°, , at pedestrian height (8.75 mm in scaled model, 1.75m in full scale).

4.3 Distribution of pollutant concentration on building surfaces

Figures 13 and 14 display the impacts of air pollutants and their distribution on the building surfaces under different incident wind angles and orientations of the building arrays.

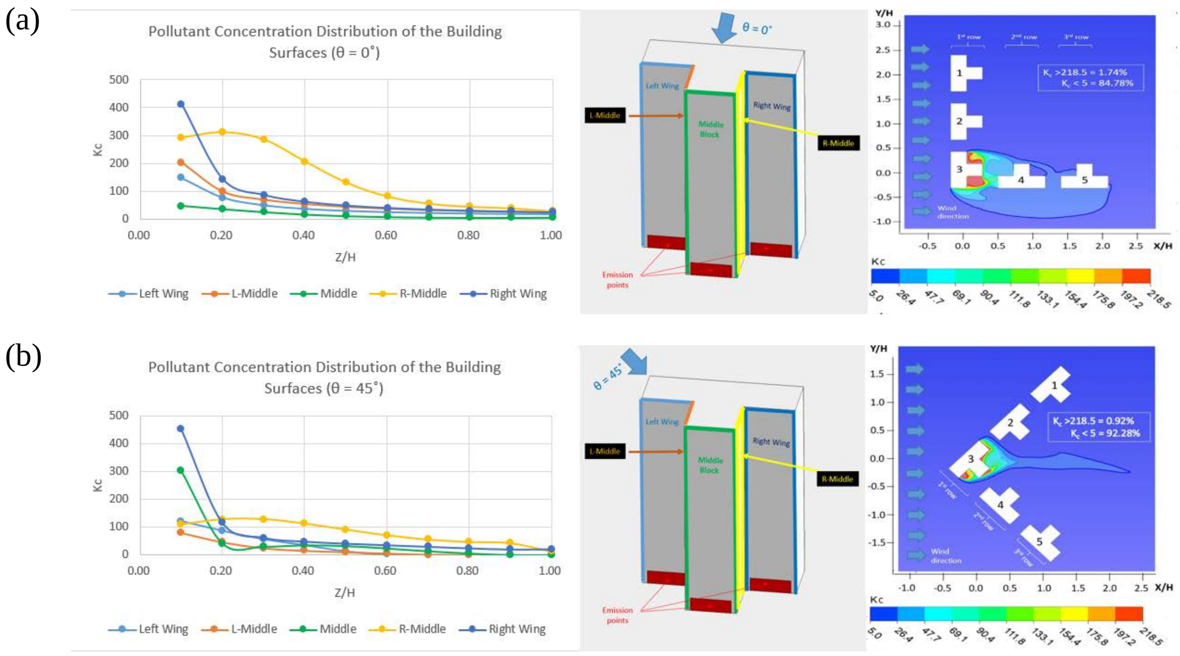

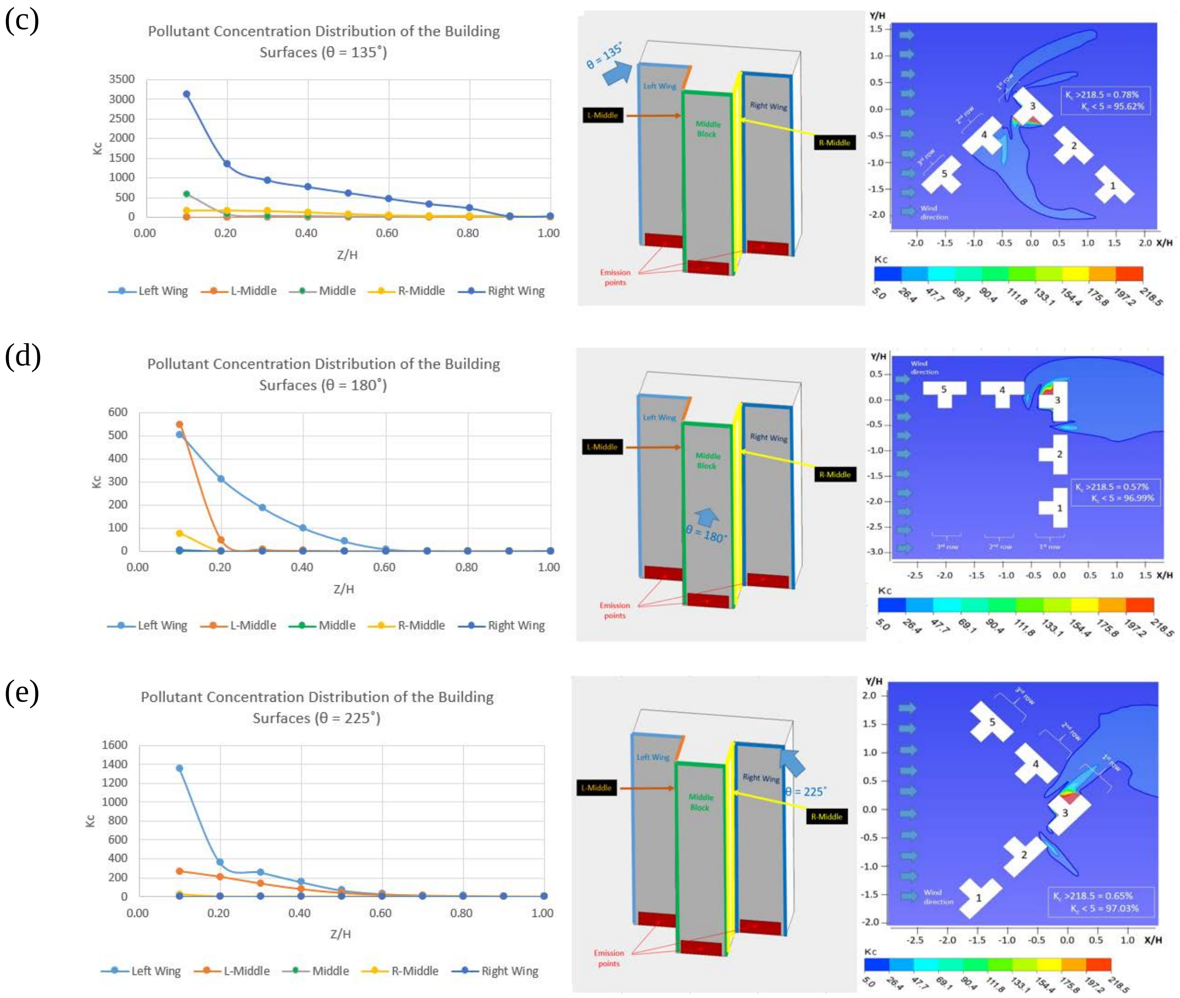

Figure 14. Distribution of pollutant concentration on the on the left wing, l-middle, middle, r-middle, and right wing building walls, under incident wind angles of: (a) 0°, (b) 45°, (c) 135°, (d) 180°, and (e) 225° in the 'L'-shaped building array.

The 'L'-shaped building array showed higher pollutant concentrations at lower levels on the building surfaces of the right wing and r-middle walls (Figure 14(a)) under an incident wind angle of 0°. A rapid decay in pollutant concentration and increase in the vertical distance from the emission points significantly reduced the pollutant concentration. The contour lines show that the horizontal distributions of pollutants at the pedestrian level and the air pressure imposed by the airflow passing through the gap between Blocks 2 and 3 suppressed the accumulation and horizontal spread of pollutants emitted from the right wing. Figure 14(b) shows that the emissions dispersed quite rapidly in the windward region, which included the left wing and middle walls of the building. The emission concentration was relatively high at lower levels on the walls of the middle block and the right wing and rapidly decayed at upper levels. All building surfaces showed a rather low pollutant concentration at lower levels for z = 0.2H. For incident winds approaching 90° (Figure 14(c)), the stagnation zone between the right wing and r-middle walls trapped air pollutants more than on other building surfaces.

The front sections of Blocks 4 and 5 blocked the airflow, making the right wing of the source building more susceptible to poor ventilation. Because the left wing is more susceptible to the blockage effect of the building blocks located upstream for incident winds approaching 180° (Figure 14(d)), the pollutant concentration at lower vertical levels was high. The rapid airflow caused by turbulence in the upper vertical levels developed between both buildings and helped dissipate air pollutants; hence, pollutant concentrations on the L-middle wall decayed rapidly. The other building surfaces were not affected by air pollutants emitted from the lower floors. For wind approaching from the opening of the building arrays from an angle of 225° (Figure 14(e)) with a downstream emission source, neighboring buildings and the central space of the building array were the least affected. The middle block obstructed the airflow and created a small air stagnation zone between the left wing and l-middle walls, increasing the air pollution concentration relative to the other walls. However, as the vertical distance from the emission source increased, the concentration of pollutants decreased to very low levels comparable to those of the other building surfaces.

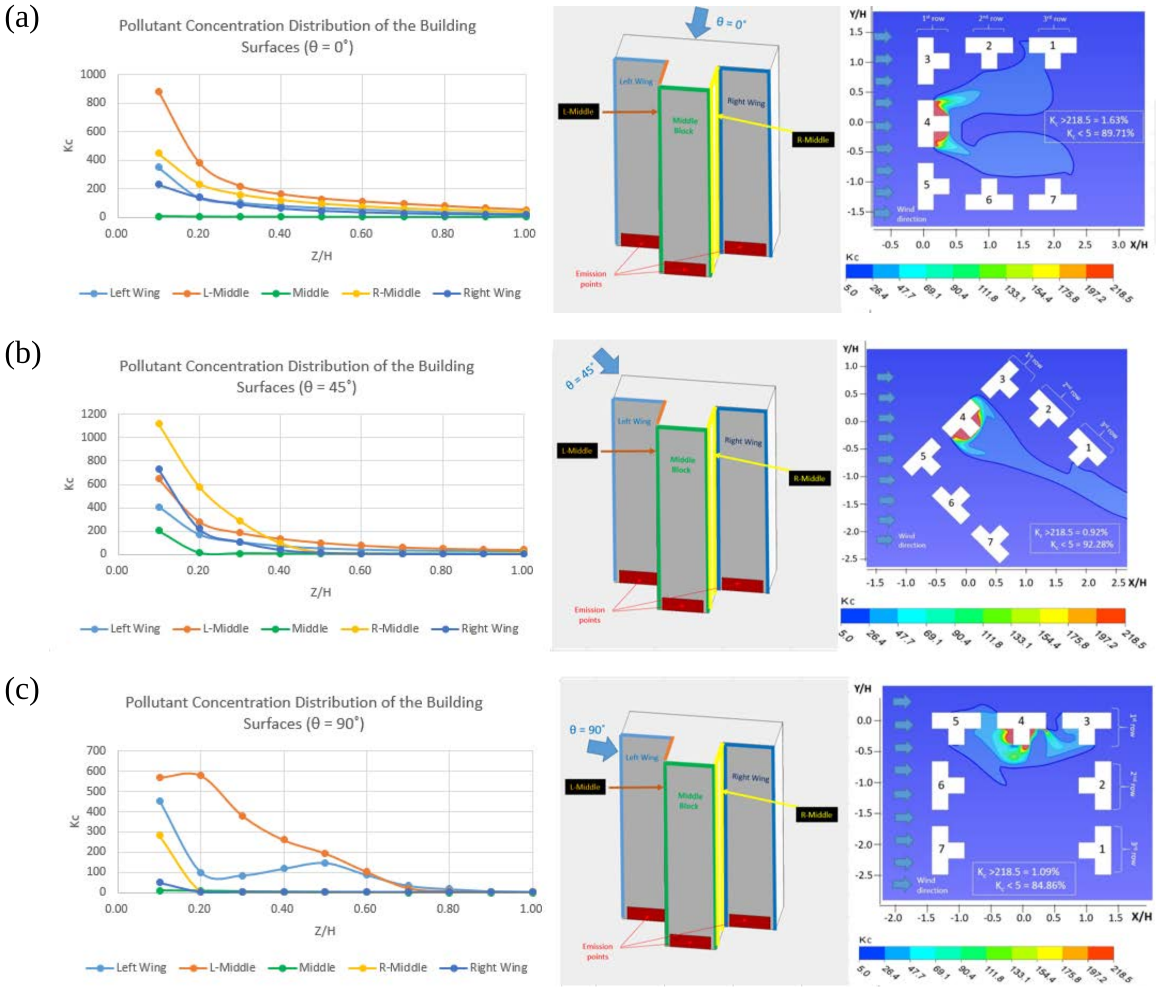

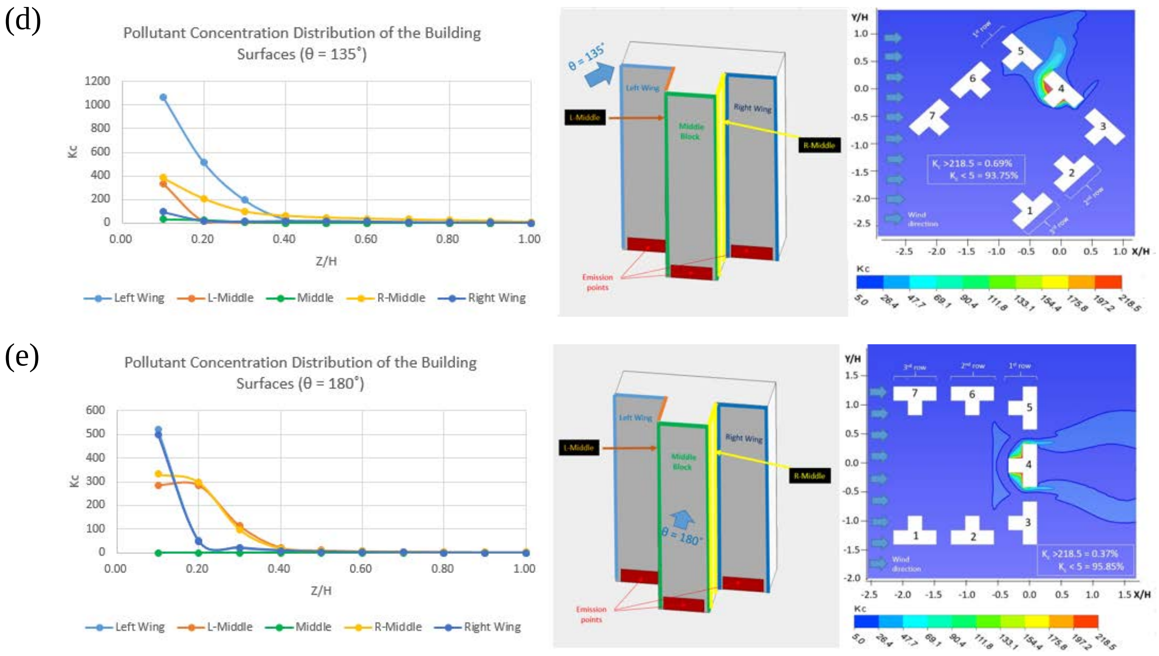

Figure 15. Distribution of pollutant concentration on the left wing, l-middle, middle, r-middle, and right wing building walls, under incident wind angles of: (a) 0°, (b) 45°, (c) 90°, (d) 135°, and (e) 180° for the ‘U’-shaped building array.

For wind approaching the ‘U’-shaped building arrays (Figure 15a) from an incident angle of 0°, the central space was affected by worst-case scenario emission concentrations. However, owing to the even and symmetrical distribution of air circulation, the concentration of air pollutants gradually decreased with the vertical height of the building. Under the oblique winds approaching from 45° (Figure 15(b)), the perturbation of turbulence created on the leeward walls of the source building (i.e., Block 4) caused various degrees of pollutant concentrations on all surfaces in the leeward direction. The rapid air movement inside the central space for an oblique wind direction gradually decreased the pollutant concentration (similar to the case in Figure 15(a) with an incident wind angle of 0°). For wind approaching from the side at 90°, the concentrations of pollutants generally dropped to relatively low levels (i.e., $K_c < 200$) when moving away from the emission source and reached z = 0.4H (see Figure 15c). However, for an incident wind angle of 90° in the ‘U’-shaped building array, pollutant concentration on the l-middle wall decayed slightly with the building height due perhaps to the blockage effect imposed by the upstream building (i.e., Block 5). Air stagnation enhanced the accumulation of air pollutants, did not cause dispersion, and accounted for the subtle increase in pollutant concentrations on the mid-level left wing wall. For an oblique wind angle of 135° under the shade of Block 6, initial pollutant concentrations on the left wing were comparatively high (Figure 15(d)). Similar to all other wall surfaces, the concentration decayed rather quickly to a very low level at a vertical height of approximately z = 0.4H. The opposite wind angle of 180° provided the most favorable conditions for pollutant dispersal in the wind direction on the leeward side of the building group (Figure 15(e)).

4.4 Limitations and future research

The primary goals of this study were to evaluate the impacts of different incident wind directions and building orientations on wind velocity and air pollutant accumulation at the pedestrian level in the central space of the buildings arranged in 'L' and 'U'-shaped arrays. Only two isolated common building arrays were assumed; thus, the distribution of airflow and dispersion of pollutants in other irregular building arrangements or within a complex urban setting with many more building shapes and arrays requires further study. In addition, to achieve the objectives of this study, the isothermal condition was assumed and investigated as a reference to evaluate the differences of wind environment at pedestrian level in the central space and the dispersion of air contaminants around buildings through the idealized building arrays. The buoyancy effect, which has not been adequately considered in this study, is an essential driving force for natural ventilation, especially when the wind speed is low inside the building arrays and within the street canyon. Niu and Tung [53] suggested that the influence of thermal force would only be overwhelmed by turbulence when the wind speed is lower than 0.9 m/s. With a temperature difference between the indoor and outdoor air, the driving force could become complicated and lead to different ventilation and pollutant dispersion results. Hence, some authors suggested considering the wall thermal boundary conditions under relatively low wind speed to achieve the correct airflow patterns, especially when the study focuses on pollutant and heat removal [54]. Another important criterion for simulating isothermal flow and dispersion fields is the Reynolds number (Re) independence. According to Re-independence theory, when the Re exceeds a critical value, the flow field would enter an Re-independent regime and the flow characteristics do not change with the increase of Re [55]. Therefore, the characteristics of the ventilation performance and pollutant dispersion in the urban environment under low wind conditions with buoyancy effect and convective heat transfer may need further study.

5. Conclusion

Incident wind angles and the orientations of building arrays arranged in 'U' and 'L' shapes (common in Hong Kong) strongly effect LWV zone development in the central space of the array and the pollutant distribution at the pedestrian level in the central space within the buildings commonly used for amenities or recreational facilities.

Incident wind angles of 0°, 45°, 135°, 180°, and 225° and 0°, 45°, 90°, 135°, and 180° were considered for ‘L’- and U’-shaped building arrays, respectively.

In conclusion, incident wind direction and the arrangement of different building arrays significantly affect ventilation and pollutant dispersion within the central space of building arrays and the building surfaces. In general, ‘L’-shaped building arrays have slightly better LWV zone area ratios and smaller areas of high pollutant concentration than ‘U’-shaped arrays. The wider opening of the array enclosure in the ‘L’-shaped array and the blockage effect posed by the buildings located downstream in the ‘U’-shaped arrangement of buildings could be contributing factors. The worst-case scenario for the proportion and distribution of the LWV and high pollutant concentration zones in the ‘L’-shaped building arrays is an incident wind of 0°, which also produces the least favorable conditions for the central space of the ‘U’-shaped arrays. Oblique wind directions favor the distribution of airflow and pollutants but depend on the opening of the semi-enclosed building array structure and the direction of the pollution source. Therefore, architects and building engineers need to consider the benefit of ‘L’-shaped arrays instead of the ‘U’-shaped arrays and avoid certain building orientations to enhance the wind comfort experienced by pedestrians enjoying recreational facilities in the central space of the buildings to achieve better ventilation and air quality.

6. Acknowledgment

This research was not supported by any grants from funding agencies in the public, commercial, or not-for-profit sectors.

7. References

[1] C. Borrego, H. Martins, O. Tchepel, L. Salmim, A. Monteiro, A.I. Miranda, How urban structure can affect city sustainability from an air quality perspective, Environmental Modelling and Software 21(4) (2006) 461-467.

[2] C. Yuan, E. Ng, L.K. Norford, Improving air quality in high-density cities by understanding the relationship between air pollutant dispersion and urban morphologies, Building and Environment 71(C) (2014) 245-258.

[3] K.Y. Lee, C.M. Mak, A comprehensive approach to study stack emissions from a research building in a small urban setting, Sustainable Cities and Society 51 (2019) 101710.

[4] Y.W. Dai, C.M. Mak, Z.T. Ai, J. Hang, Evaluation of computational and physical

parameters influencing CFD simulations of pollutant dispersion in building arrays, Building and Environment 137 (2018) 90-107.

[5] Z.T. Ai, C.M. Mak, CFD simulation of flow in a long street canyon under a perpendicular wind direction: Evaluation of three computational settings, Building and Environment 114 (2017) 293-306.

[6] L.W. Chew, L.K. Norford, Pedestrian-level wind speed enhancement in urban street canyons with void decks, Building and Environment 146 (2018) 64-76.

[7] Z.T. Ai, C.M. Mak, From street canyon microclimate to indoor environmental quality in naturally ventilated urban buildings: Issues and possibilities for improvement, Building and Environment 94 (2015) 489-503.

[8] Z.T. Ai, C.M. Mak, H.C. Lee, Roadside air quality and implications for control measures: A case study of Hong Kong, Atmospheric Environment 137 (2016) 6-16.

[9] Z.S. Fang, X.W. Feng, J.L. Liu, Z. Lin, C.M. Mak, J.L. Niu, K.T. Tse, X.N. Xu, Investigation into the differences among several outdoor thermal comfort indices against field survey in subtropics, Sustainable Cities and Society 44 (2019) 676-690.

[10] N.P. Gao, J.L. Niu, M. Perino, P. Heiselberg, The airborne transmission of infection between flats in high-rise residential buildings: Tracer gas simulation, Building and Environment 43(11) (2008) 1805-1817.

[11] M.Y. Tsai, K.S. Chen, Measurements and three-dimensional modeling of air pollutant dispersion in an Urban Street Canyon, Atmospheric Environment 38(35) (2004) 5911-5924.

[12] J.S. Wang, T.L. Chan, C.S. Cheung, C.W. Leung, W.T. Hung, Three-dimensional pollutant concentration dispersion of a vehicular exhaust plume in the real atmosphere, Atmospheric Environment 40(3) (2006) 484-497.

[13] K.W. Chen, L. Norford, Evaluating Urban Forms for Comparison Studies in the Massing Design Stage, Sustainability 9(6) (2017) 987.

[14] Y.D. Huang, X.N. Hu, N.B. Zeng, Impact of wedge-shaped roofs on airflow and pollutant dispersion inside urban street canyons, Building and Environment 44(12) (2009) 2335-2347.

[15] S.H.L. Yim, J.C.H. Fung, A.K.H. Lau, S.C. Kot, Air ventilation impacts of the "wall effect" resulting from the alignment of high-rise buildings, Atmospheric Environment

43(32) (2009) 4982-4994.

[16] Y. Jiang, D. Alexander, H. Jenkins, R. Arthur, Q.Y. Chen, Natural ventilation in buildings: measurement in a wind tunnel and numerical simulation with large-eddy simulation, Journal of Wind Engineering and Industrial Aerodynamics 91(3) (2003) 331-353.

[17] M.Á. Padilla-Marcos, A. Meiss, J. Feijó-Muñoz, Proposal for a simplified CFD procedure for obtaining patterns of the age of air in outdoor spaces for the natural ventilation of buildings, Energies 10(9) (2017) 1252.

[18] B. Blocken, T. Stathopoulos, J.P.A.J. van Beeck, Pedestrian-level wind conditions around buildings: Review of wind-tunnel and CFD techniques and their accuracy for wind comfort assessment, Building and Environment 100 (2016) 50-81.

[19] Y.X. Du, C.M. Mak, J.L Liu, Q. Xia, J.L. Niu, K.C.S. Kwok, Effects of lift-up design on pedestrian level wind comfort in different building configurations under three wind directions, Building and Environment 117 (2017) 84-99.

[20] A. Mochida, I.Y.F. Lun, Prediction of wind environment and thermal comfort at pedestrian level in urban area, Journal of Wind Engineering and Industrial Aerodynamics 96(10) (2008) 1498-1527.

[21] R. Yoshie, A. Mochida, Y. Tominaga, H. Kataoka, K. Harimoto, T. Nozu, T. Shirasawa, Cooperative project for CFD prediction of pedestrian wind environment in the Architectural Institute of Japan, Journal of Wind Engineering and Industrial Aerodynamics 95(9) (2007) 1551-1578.

[22] M. Lin, J. Hang, Y. Li, Z. Luo, M. Sandberg, Quantitative ventilation assessments of idealized urban canopy layers with various urban layouts and the same building packing density, Building and Environment 79 (2014) 152-167.

[23] F. Yang, Y. Gao, K. Zhong, Y. Kang, Impacts of cross-ventilation on the air quality in street canyons with different building arrangements, Building and Environment 104 (2016) 1-12.

[24] Z.T. Ai, C.M. Mak, J.L. Niu, Numerical investigation of wind-induced airflow and interunit dispersion characteristics in multistory residential buildings, Indoor Air 23(5) (2013) 417-429.

[25] D.J. Cui, C.M. Mak, K.C.S. Kwok, Z.T. Ai, CFD simulation of the effect of an upstream building on the inter-unit dispersion in a multi-story building in two wind directions,

Journal of Wind Engineering and Industrial Aerodynamics 150 (2016) 31-41.

[26] J.L Liu, J.L Niu, Y. Du, C.M. Mak, Y.F. Zhang, LES for pedestrian level wind around an idealized building array—Assessment of sensitivity to influencing parameters, Sustainable Cities and Society 44 (2019) 406-415.

[27] C.K.C. Cheng, K.M. Lam, Y.T.A. Leung, K. Yang, H.W. Li Danny, C.P. Cheung Sherman, Wind-induced natural ventilation of re-entrant bays in a high-rise building, Journal of Wind Engineering and Industrial Aerodynamics 99(2) (2011) 79-90.

[28] W.D. Janssen, B. Blocken, T. van Hooff, Pedestrian wind comfort around buildings: Comparison of wind comfort criteria based on whole-flow field data for a complex case study, Building and Environment 59 (2013) 547-562.

[29] Q.M. Zahid Iqbal, A.L.S. Chan, Pedestrian level wind environment assessment around group of high-rise cross-shaped buildings: Effect of building shape, separation and orientation, Building and Environment 101 (2016) 45-63.

[30] K.Y. Lee, C.M. Mak, Effects of different wind directions on ventilation of surrounding areas of two generic building configurations in Hong Kong, Indoor and Built Environment (2021) 1420326X211016040.

[31] V. Cheng, E. Ng, Thermal Comfort in Urban Open Spaces for Hong Kong, Architectural Science Review 49(3) (2006) 236-242.

[32] E. Ng, I. Tam, A. Ng, B. Givoni, L. Katzschner, K. Kwok, V. Cheng, Feasibility study for establishment of air ventilation assessment system–final report, Hong Kong: Department of Architecture, Chinese University of Hong Kong 16 (2005).

[33] B. Leitl, M. Schatzmann, Compilation of experimental data for validation purposes, Meteorology Institute, Hamburg University, Hamburg, 1998.

[34] K. An, J.C.H. Fung, S.H.L. Yim, Sensitivity of inflow boundary conditions on downstream wind and turbulence profiles through building obstacles using a CFD approach, Journal of Wind Engineering and Industrial Aerodynamics 115 (2013) 137-149.

[35] J.L. Liu, J.L. Niu, Y.X. Du, C.M. Mak, Y.F. Zhang, LES for pedestrian level wind around an idealized building array—Assessment of sensitivity to influencing parameters, Sustainable Cities and Society 44 (2019) 406-415.

[36] Q. Xia, J.L. Niu, X.P. Liu, Dispersion of air pollutants around buildings: A review of

past studies and their methodologies, London, England, 2014, pp. 201-224.

[37] B. Blocken, Computational Fluid Dynamics for urban physics: Importance, scales, possibilities, limitations and ten tips and tricks towards accurate and reliable simulations, Building and Environment 91 (2015) 219-245.

[38] M. Lateb, C. Masson, T. Stathopoulos, C. Bedard, Comparison of various types of k- epsilon models for pollutant emissions around a two-building configuration, Journal of Wind Engineering and Industrial Aerodynamics 115(C) (2013) 9-21.

[39] Y. Tominaga, T. Stathopoulos, Numerical simulation of dispersion around an isolated cubic building: Comparison of various types of k–ε models, Atmospheric Environment 43(20) (2009) 3200-3210.

[40] P.W. Tien, J.K. Calautit, Numerical analysis of the wind and thermal comfort in courtyards “skycourts” in high rise buildings, Journal of Building Engineering 24 (2019) 100735.

[41] Z.T. Ai, C.M. Mak, A study of interunit dispersion around multistory buildings with single-sided ventilation under different wind directions, Atmospheric Environment 88 (2014) 1-13.

[42] J.L. Liu, J.L. Niu, CFD simulation of the wind environment around an isolated high-rise building: An evaluation of SRANS, LES and DES models, Building and Environment 96(C) (2016) 91-106.

[43] Y.X. Du, C.M. Mak, Y.T. Li, A multi-stage optimization of pedestrian level wind environment and thermal comfort with lift-up design in ideal urban canyons, Sustainable Cities and Society 46 (2019) 101424.

[44] ANSYS FLUENT 14.5, ANSYS, Inc., Canonsburg, PA, USA, 2012.

[45] R. Meroney, Wind tunnel and numerical simulation of pollution dispersion: a hybrid approach, Paper for Invited Lecture at the Croucher Advanced Study Institute, Hong Kong University of Science and Technology (2004) 6-10.

[46] Y. Abu-Zidan, P. Mendis, T. Gunawardena, Impact of atmospheric boundary layer inhomogeneity in CFD simulations of tall buildings, Heliyon 6(7) (2020) e04274.

[47] Z.T. Ai, C.M. Mak, CFD simulation of flow and dispersion around an isolated building: Effect of inhomogeneous ABL and near-wall treatment, Atmospheric Environment 77 (2013) 568-578.

[48] C. Gorlé, J. van Beeck, P. Rambaud, Dispersion in the Wake of a Rectangular Building: Validation of Two Reynolds-Averaged Navier–Stokes Modelling Approaches, Boundary-Layer Meteorology 137(1) (2010) 115-133.

[49] B. Blocken, T. Stathopoulos, J. Carmeliet, CFD simulation of the atmospheric boundary layer: wall function problems, Atmospheric Environment 41(2) (2007) 238-252.

[50] J. Franke, A. Hellsten, H. Schlünzen, B. Carissimo, Cost Action 732: Best practice guideline for the CFD simulation of flow in the urban environment, in: Quality assurance and impovement of microscale meteorological models,, Meteorological Inst., Brussels, 2007.

[51] Y. Tominaga, A. Mochida, R. Yoshie, H. Kataoka, T. Nozu, M. Yoshikawa, T. Shirasawa, AIJ guidelines for practical applications of CFD to pedestrian wind environment around buildings, Journal of Wind Engineering and Industrial Aerodynamics 96(10) (2008) 1749-1761.

[52] H. Montazeri, B. Blocken, CFD simulation of wind-induced pressure coefficients on buildings with and without balconies: Validation and sensitivity analysis, Building and Environment 60 (2013) 137-149.

[53] J.L Niu, T.C.W. Tung, On-site quantification of re-entry ratio of ventilation exhausts in multi-family residential buildings and implications, Indoor air 18(1) (2008) 12-26.

[54] G.X. Chen, L. Rong, G.Q. Zhang, Comparison of urban airflow between solar-induced thermal wall and uniform wall temperature boundary conditions by coupling CitySim and CFD, Building and Environment 172 (2020) 106732.

[55] W.H. Snyder, Guideline for fluid modeling of atmospheric diffusion. Fluid modeling report no. 10, in: E.P. Agency. (Ed.) Research Triangle Park, NC (USA). Environmental Sciences Research Lab., 1981.